Pressure Tensor Elements Breaking the Frozen-In Law During Reconnection in Earth's Magnetotail

J. Egedal,[1] J. Ng,[2] A. Le,[3] W. Daughton,[3] B. Wetherton,[1] J. Dorelli,[4] D. Gershman,[4] and A. Rager[4]
[1]Department of Physics, University of Wisconsin-Madison, Madison, Wisconsin 53706, USA
[2]Center for Heliophysics, Princeton Plasma Physics Laboratory, Princeton, New Jersey 08543, USA
[3]Los Alamos National Laboratory, Los Alamos, New Mexico 87545, USA
[4]Heliophysics Science Division, NASA Goddard Space Flight Center, Greenbelt, Maryland 20771, USA

(Received 20 December 2018; revised manuscript received 22 August 2019; published 25 November 2019)

Aided by fully kinetic simulations, spacecraft observations of magnetic reconnection in Earth's magnetotail are analyzed. The structure of the electron diffusion region is in quantitative agreement with the numerical model. Of special interest, the spacecraft data reveal how reconnection is mediated by off-diagonal stress in the electron pressure tensor breaking the frozen-in law of the electron fluid.

DOI: 10.1103/PhysRevLett.123.225101

Magnetic reconnection is the process that breaks and rearranges the connectivity of magnetic field lines in plasmas [1]. Plasmas, which are generally excellent conductors of electrical currents, are abundant throughout the universe, and magnetic reconnection is believed to be fundamental to a range of phenomena in astrophysical and laboratory settings where large scale current layers become unstable and explosively release their magnetic field energy [2,3]. The plasma frozen-in law of magnetohydrodynamics (MHD) states that a perfectly conducting plasma with ion fluid velocity $\mathbf{u}_i$ cannot support an electric field in its own frame of reference, i.e., $\mathbf{E}+\mathbf{u}_i\times\mathbf{B}=\mathbf{0}$. During reconnection, the inertia of the ions breaks this law within ion diffusion regions (IDRs) at the length scale, $d_i=c/\omega_{pi}=\sqrt{m_i/(\mu_0 n_e e^2)}$. For the magnetotail (considered here) this ion inertial scale is relatively large, $d_i\simeq 10^3$ km. Reconnection, however, also requires the decoupling of the electron motion from the magnetic fields, and theoretical studies of magnetic reconnection are often concerned with how the more restrictive frozen-in law $\mathbf{E}'\equiv\mathbf{E}+\mathbf{u}_e\times\mathbf{B}=\mathbf{0}$ for the electron fluid with bulk velocity $\mathbf{u}_e$, is violated within much smaller electron diffusion regions (EDRs).

Theories have been proposed advocating that 3D effects or turbulence may cause local suppression of the effective conductivity, permitting reconnection to proceed at the fast rates observed [4]. However, under conditions typical of magnetospheric reconnection, 3D effects have been found to be relatively unimportant for suppressing the conductivity, even in asymmetric current sheets where these effects are stronger [5–7]. Rather, 2D and 3D kinetic models suggest that $\mathbf{E}'\neq\mathbf{0}$ can be caused by stress in the electron pressure tensor becoming important when the spatial scale length of the EDR reaches the electron inertial scale, $d_e=c/\omega_{pe}\simeq d_i/43$ [8–13].

NASA's Magnetospheric Multiscale (MMS) mission [14] was specially designed to characterize the fine scale structure of magnetic reconnection in Earth's magnetosphere and has successfully recorded reconnection events for a range of environments in the magnetosphere [15]. These include asymmetric reconnection events in the dayside magnetopause [16], where electron beams oblique to the magnetic lines of force break the frozen-in law [17]. However, so far, no direct observations have been reported on how the electron frozen-in law is broken during symmetric reconnection in the magnetotail. In this Letter we use fully kinetic simulation results to aid a detailed analysis of the EDR encounter reported by Torbert *et al.* [18], and examine the mechanism responsible for breaking the electron frozen-in law.

Similar to previous studies of spacecraft reconnection events [19,20] our analysis is aided by kinetic simulations, providing a first principles model for the reconnection dynamics. At each time step of a simulation, the velocities and positions for a large number of numerical particles (we used $\simeq 10^{10}$) are updated according to Newton's second law applied with forces from the electromagnetic fields. The fields, in turn, are computed self-consistently from the distributions of charges and currents carried by the particle populations. The simulation domain is spanned by the L and N coordinates. For numerical tractability we apply the common so-called 2.5D assumption where fields and particle flows are 3D vector quantities but all quantities are assumed to have vanishing gradients, $\partial/\partial M=0$, in the direction, M, normal to the LN plane.

The simulation performed with the VPIC code [21] implemented the full proton to electron mass ratio $m_i/m_e=1836$, permitting a direct mapping between all dimensionless VPIC units and spacecraft units. By imposing that the fundamental quantities of a quasineutral plasma are equivalent in the two systems and applying two scaling

factors to match the VPIC and MMS electron number densities and temperatures, there then exist a unique mapping from all dimensionless VPIC units to the units applied by the MMS spacecraft [22]. This mapping facilitates the presented quantitative comparison between the spacecraft observations and simulation data.

An important part of the spacecraft data analysis is to establish the appropriate LMN coordinate basis of the reconnection event. Here the reconnecting magnetic field component is in the L direction, while M again is the out-of-plane direction often identified by a search for a direction where plasma parameters have minimum variance [23]. However, because the MMS spacecraft did not sample the upstream plasma (located at large $|N|$) the standard methods for establishing the LMN basis of the event are not accurate. Instead, we applied an optimization approach aided by the kinetic simulation [22], yielding the basis given in the caption of Fig. 1.

The time histories for a range of quantities recorded during the MMS encounter with the EDR on July 11, 2017 are shown in Figs. 1(a)–1(k), where the red (blue) lines represent observations by MMS1 (MMS3). Estimated trajectories of the MMS spacecraft through profiles of a fully kinetic simulation are shown in Figs. 2(b)–2(e). Evaluating numerical quantities along these trajectories yields the cuts through the simulation data shown in Figs. 1(l)–1(v). Uncertainty ranges for both MMS and VPIC data are indicated in pink. Outside the reconnection region the gradient length scale is in general larger than the spacecraft separation and differences between the fully independent measurements by the various spacecraft can be applied for a conservative error estimate. Thus, for each MMS quantity, S_{MMS}, we estimate the uncertainty as the root-mean-square (RMS) of differences between the signals of MMS1 and MMS3 during the interval $-3s < t < -2s$ just outside the EDR within the tailward exhaust, i.e., $\Delta S_{\mathrm{MMS}} = \pm\sqrt{\langle (S_{\mathrm{MMS1}} - S_{\mathrm{MMS3}})^2 \rangle_t}$. For the VPIC data the main source of error is due to the $\Delta N \simeq 0.6 d_e$ uncertainty in the N coordinate along the inferred MMS trajectory, such that $\Delta S_{\mathrm{VPIC}} \simeq \pm \Delta N \partial S/\partial N$.

The trajectory of the MMS spacecraft through the simulation was reconstructed mainly using B_L and B_N from MMS1 [red lines in Figs. 1(d) and 1(f)] in relation to the VPIC profiles in Figs. 2(b) and 2(c), and included an optimization process [22] determining other free parameters of the problem (see caption). The displacement of MMS3 in the N direction relative to the other spacecraft amounts to 12 km $\sim 0.4 d_e$, and is indicated by the slight separation of the black and red trajectories in Figs. 2(b) and 2(e). The fluctuations in N along the trajectories, slow compared to the electron dynamics, are dictated by the variations in B_L.

Figure 2(d) shows color contours of the temperature ratio $T_{e\parallel}/T_{e\perp}$, where $\parallel$ and $\perp$ refer to the directions parallel and perpendicular to the local magnetic field. The EDR with $T_{e\parallel}/T_{e\perp} \simeq 1$ separates the two inflow regions each with

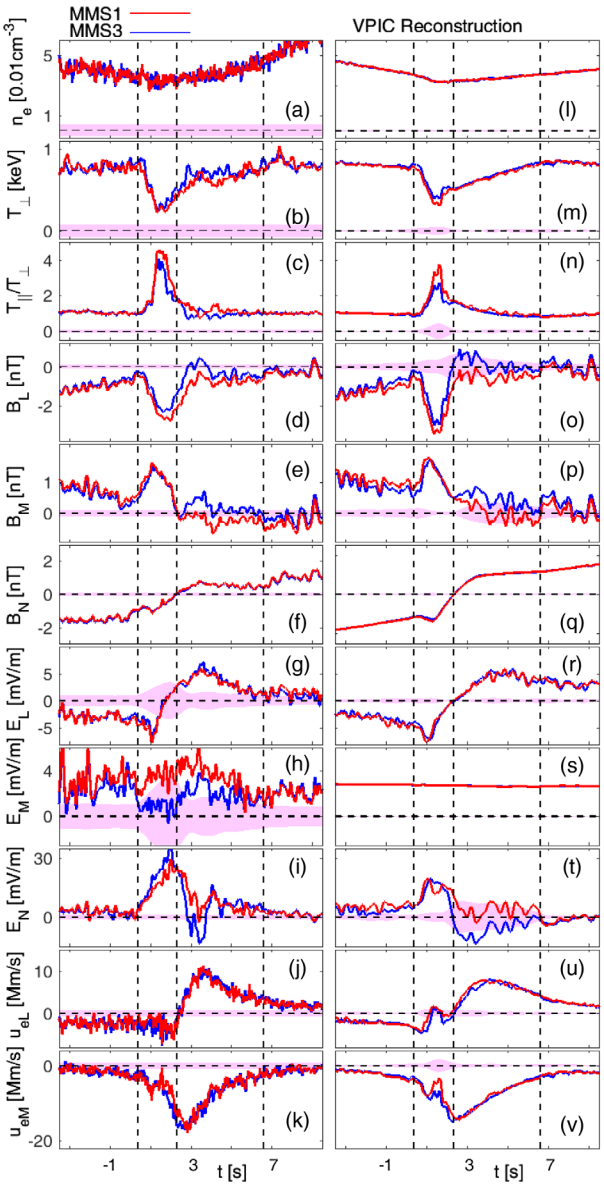

FIG. 1. (a)–(k) MMS1 (red lines) and MMS3 (blue lines) measurements of a range of quantities during the July 11, 2017 EDR encounter, with $t = 0s$ corresponding to 22:34:00 UT. The raw data provided by MMS are translated to the LMN coordinates of the event determined in the Supplemental Material [22]. In geocentric solar ecliptic (GSE) coordinates, our unit vectors $[\mathbf{L};\mathbf{M};\mathbf{N}]$ are $[0.94, -0.35, -0.03; 0.32, 0.90, -0.33; 0.15, 0.30, 0.94]$. (l)–(v) Matching simulation quantities evaluated along the trajectories shown in Fig. 2. Error estimates are shown in pink and the VPIC results are translated to MMS units and plotted with axis settings identical to those of (a)–(k).

$T_{e\parallel} \simeq 5 T_{e\perp}$. The dynamics responsible for $T_{e\parallel} \gg T_{e\perp}$ are well understood [25–27], tied to the parallel acceleration potential $\Phi_\parallel$ defined in Ref. [28] and the trapped orbit dynamics that are both displayed in Fig. 2(a) [29–32]. The spike of pressure anisotropy in Figs. 1(c) and 1(d) is

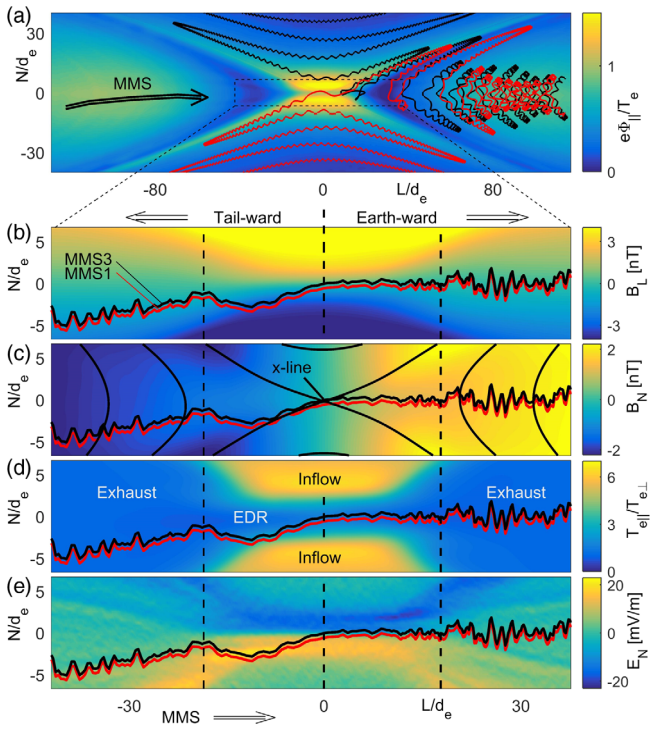

FIG. 2. Numerical profiles of $e\Phi_{\parallel}/T_e$, B_L, B_N $T_{e\parallel}/T_{e\perp}$, and E_N. Trapped electron trajectories are shown in (a), while the reconstructed path of the MMS spacecraft through the simulation is shown by the red (MMS1) and black (MMS3) lines in (b)–(e). Length scales are normalized by $d_e \simeq 29$ km calculated using the VPIC density $n/n_0 = 0.75$ observed at the x line. Here n_0 is the initial density in the center of the simulation domain. For the simulation, open boundary conditions were applied [24] on a domain of total size of 4032×4032 cells $= 10d_i \times 10d_i \simeq 428d_e \times 428d_e$, initialized with approximately 800 particles per species per cell. Other parameters determined to be consistent with the observations [22] include ratios of upstream electron and ion pressure to magnetic pressure of $\beta_{e\infty} = 0.045$ and $\beta_{i\infty} = 0.45$. Also, our optimization scheme [22] led to the inclusion of a small out of plane guide magnetic field $B_g/B_0 = 0.006$, here normalized by the initial upstream reconnection magnetic field.

consistent with the MMS trajectory in Fig. 2(d) briefly making contact with the inflow. The level of pressure anisotropy is consistent with a regime I event [33], where the marginal fire hose condition $n_e(T_{e\parallel} - T_{e\perp}) \simeq B^2/\mu_0$ is approached along the edge of the EDR, driving the extended electron outflow jets [26].

Quantitative agreement is also observed between the MMS and VPIC profiles of the electric fields, including the sharp details of E_L in Figs. 1(g) and 1(r) for $t \simeq 1s$. The E_N MMS measurement in Fig. 1(i) reaches a larger maximum value than seen in the simulation profiles in Fig. 1(t). Nevertheless, the measurement of $E_N < 0$ by MMS3 at $t \simeq 4$ s is consistent with the profiles of E_N in Fig. 2(e) where E_N abruptly changes sign at $N = 0$, indicating (in agreement with the B_L measurements) that here MMS1 and MMS3 are straddling the middle of the reconnection layer, $N = 0$.

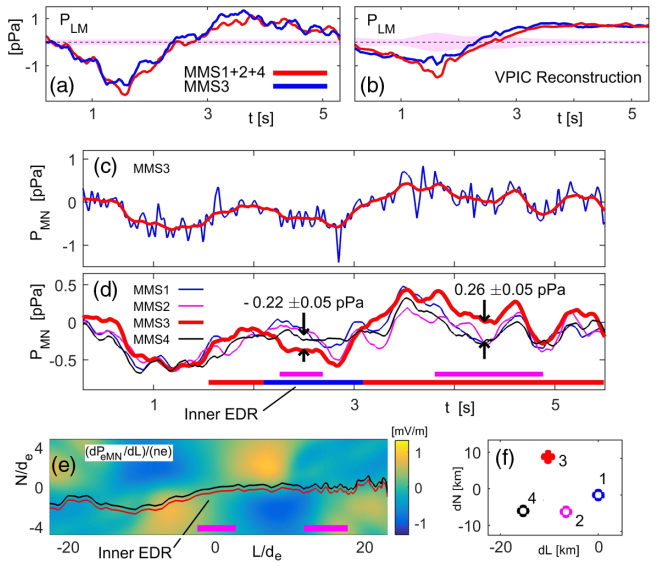

FIG. 3. In (a) and (b) the MMS and VPIC profiles of P_{LM} are shown in the format of Fig. 1. In (c) the blue line is the raw P_{MN} signal provided by MMS3, while the red line is the same signal low-pass filter at $\lesssim 4$ Hz [the same filter was also for the lines in (a)]. In (d) low-pass filtered signals of P_{MN} are shown for all MMS spacecraft. Given the VPIC structure of $\partial P_{MN}/\partial L$ in (e) and the MMS constellation in (f), from the lines in (d) we can deduce a MMS profile of $\partial P_{MN}/\partial N$ and estimate its error range [see text and Fig. 4(e)].

Spacecraft measurement of $\mathbf{E}$ is challenging and there is often some uncertainty associated with the direction of $\mathbf{E}$. The strong E_N inside the EDR can therefore influence the measurements of the weaker E_M and E_L components. In particular, by including an additional 5% of $|E_N|$ on the E_M uncertainty estimates we may account for the deviation between the E_M traces recorded by MMS1 and MMS3. The E_M measurements then also agree with the constant level of $E_M \simeq 3$ mV/m seen in the VPIC run within the range of uncertainty, and values reported for E_M in Refs. [34,35]. Finally, quantitative agreement is also observed for the electron flow profiles in Figs. 1(l), 1(k), 1(u), 1(v), where the MMS trajectory largely missed the electron jets in the negative L direction.

Next, with Figs. 3 and 4 we seek to demonstrate how the MMS spacecraft directly captured the physical mechanism responsible for breaking the frozen-in law discussed above, $\mathbf{E}' = \mathbf{E} + \mathbf{u}_e \times \mathbf{B} = \mathbf{0}$. At the center of the reconnection site the lines of the in-plane magnetic field meet in an x configuration, where the center point is known as the x point. In 3D the x points form a continuous line denoted the x line, which in our 2D representation is the line in the M direction characterized by $L = N = 0$ [see Fig. 2(c)]. The electric field along the x line is of special importance as, by Faraday's law, it describes the rate at which magnetic flux convects across this line defining the magnetic topology. $\mathbf{E}$ along the x line (in our case E_M) is therefore a direct measure of the reconnection rate.

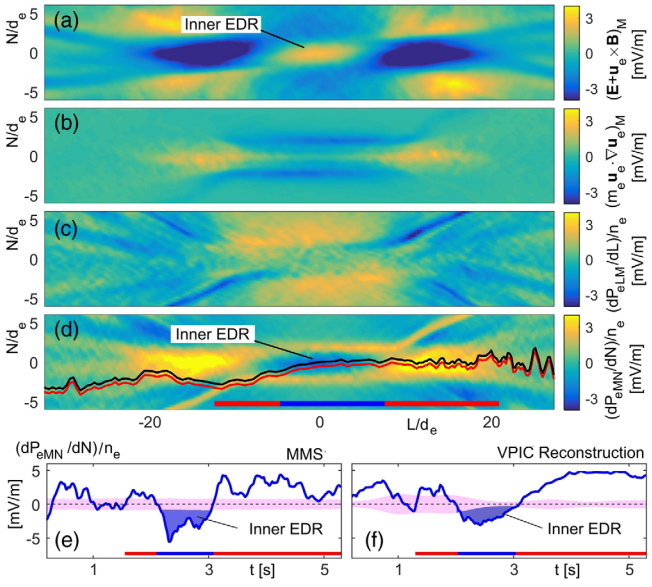

FIG. 4. (a)–(d) Color contours of terms important for the electron momentum balance in the M direction. (e),(f) Matching profiles of MMS and VPIC pressure tensor term $(\partial p_{eMN}/\partial N)/ne$, where the MMS profile is obtained from the curves in Fig. 3(d). The ranges of error are shown in pink, determined as described in the text, and are consistent with quantitative agreement between MMS and VPIC signals within the inner EDR.

A momentum equation for the electron fluid that retains additional physical effects similar to those described by the Navier-Stokes equation of regular fluid mechanics can be obtained from plasma kinetic theory. Under collisionless conditions and neglecting partial time derivative terms, this generalized Ohm's law takes the form

$$\mathbf{E} + \mathbf{u}_e \times \mathbf{B} + \frac{1}{ne}\nabla \cdot \mathbf{p}_e + \frac{m_e}{e}\mathbf{u}_e \cdot \nabla \mathbf{u}_e = 0. \quad (1)$$

Here the kinetic effects are retained through the term involving the electron pressure tensor $\mathbf{p}_e = m_e \int (\mathbf{v}-\mathbf{u}_e)(\mathbf{v}-\mathbf{u}_e) f_e(\mathbf{v}) d^3v$. The last term, $m_e \mathbf{u}_e \cdot \nabla \mathbf{u}_e/e$, is the electron inertial force against acceleration proportional to the convective time derivative of $m_e \mathbf{u}_e$.

For the present case of symmetric reconnection the electron inertia vanishes at the x line. For 2D configurations Eq. (1) then implies that $(\nabla \cdot \mathbf{p})_M = \partial p_{eLM}/\partial L + \partial p_{eMN}/\partial N$, are the only two terms that can break the frozen-in law, permitting E_M to remain finite along the x line. The MMS and VPIC reconstructed traces of p_{eLM} are shown in Figs. 3(a) and 3(b), both including a steady ramp of $\Delta p_{eLM} = 3$ pPa over a distance of $\Delta L \simeq 15 d_i \simeq 500$ km centered on the inner reconnection region at $t \simeq 2.5$ s. We then have $(\partial p_{eLM}/\partial L)/(en) \simeq +1$ mV/m adding in Eq. (1) to the value of E_M.

To evaluate $\partial p_{eMN}/\partial N$ and its experimental uncertainty we consider data from all four spacecraft. In Fig. 3(c) the blue line is the raw p_{eMN} signal of MMS3, while the red line provides the low-pass filtered ($\lesssim 4$ Hz) signal reducing the noise caused in part by limited counting statistics on the MMS electron detectors. This filtered signal is repeated in Fig. 3(d) together with those recorded by MMS1,2,4. The differences between these signals are related to the spatial constellation of the MMS tetrahedron which in Fig. 3(f) is projected on the LN plane. Given MMS1,2,4 all have small N separation their recorded value of p_{eMN} should be similar in regions where $\partial p_{eMN}/\partial L$ is small. Intervals of $\partial p_{eMN}/\partial L \simeq 0$ are identified by the magenta bars in the VPIC profile in Fig. 3(e) and, indeed, during these intervals [highlighted by the similar magenta bars in Fig. 3(d)] MMS1,2,4 recorded values of p_{eMN} that agree within ± 0.05 pPa, providing a direct error estimate on the p_{eMN} measurement inside the EDR. In turn, this error estimate agrees with that provided by the RMS method described above.

In Fig. 3(d) the red line of p_{eMN} by MMS3 displays a statistically significant deviation from the lines of the other spacecraft. Given the $\Delta N \simeq 12$ km separation of MMS3 relative to MMS1,2,4 we interpret this deviation as a measure of $\Delta N \partial P_{eMN}/\partial N$. At the inner EDR, we observe $\Delta P_{eMN} = -0.22 \pm 0.05$ pPa such that here $(\partial P_{eMN}/\partial N)/ne \simeq -0.22$ pPa$/(12$ km 0.032 cm^{-3} 1.6×10^{-19} C$) \simeq -3.6 \pm 0.8$ mV/m, with the full trace of $(\partial P_{eMN}/\partial N)/ne$ shown in Fig. 4(e). In addition, the red-blue-red bars in Fig. 3(d) and Figs. 4(d)–4(f) indicate where $\partial p_{eMN}/\partial N$ is positive-negative-positive, with the negative interval centered on the inner EDR.

The VPIC profiles of the terms in Eq. (1) are shown in Fig. 4. In panel (a) the two most negative blue regions where $(\mathbf{E} + \mathbf{u}_e \times \mathbf{B})_M \simeq -5$ mV/m are caused by the strong outflow electron jets moving faster than the magnetic field lines. Profiles of the electron inertia term and stress component $(\partial p_{eLM}/\partial L)/(en)$ are shown in (b) and (c), respectively. While these profiles have interesting structures they are relatively unimportant within the inner EDR to the momentum balance of Eq. (1). This is in contrast to the profile of $(\partial P_{eMN}/\partial N)/ne$ shown in (d), which is anticorrelated with the profile in (a), such that their sum is approximately zero (not shown) throughout the region. Evaluating the profile in (d) along the MMS trajectory we obtain the VPIC reconstructed trace shown in (f).

We can now combine the evidence from the MMS data revealing the mechanism that breaks the electron frozen-in law. As was the case for all other quantities examined above, in Figs. 4(e) and 4(f) we observed a quantitative agreement between the MMS and the VPIC signals for $(\partial P_{eMN}/\partial N)/ne$. In particular, within the inner EDR both MMS and VPIC data display values which are significantly beyond their range of uncertainty [blue shaded regions in (e) and (f)]. Consistent with force balance along the x line the combined force (per charge) of $E_M + (\partial P_{eLM}/\partial L)/ne = (3 \pm 0.8) + (1 \pm 0.2) = 4 \pm 1$ mV/m is offset by $(\partial P_{eMN}/\partial N)/ne \simeq -3.6 \pm 0.8$ mV/m, hereby breaking

the frozen-in law. The error ranges are conservatively based on the pink shaded ranges in the figures.

In summary, a detailed analysis of MMS observations of symmetric magnetic reconnection in Earth's magnetotail is presented and compared to results from 2D fully kinetic simulations. With the numerical run applying the full proton-electron mass ratio, $m_i/m_e = 1836$, the simulation units can be mapped directly to the units of the MMS measurements. In turn, for fixed LMN coordinates the B_L and B_N measurements then determine the MMS trajectory through the simulation domain, yielding the demonstrated quantitative agreement for all simulation parameters compared with the observations. Based on an examination of the electron force balance equation, it is concluded that the off-diagonal stress term $(\partial p_{eMN}/\partial N)/ne$ is responsible for breaking the frozen-in condition for the electrons and is consistent with rate of reconnection in this naturally occurring magnetotail event.

We thank the MMS Science Data Center [36] for providing the data for this study. Simulations used LANL Institutional Computing and NASA HEC resources. A. L. acknowledges NASA Grant No. NNH17AE361.

[1] J. Dungey, Philos. Mag. **44**, 725 (1953).
[2] S. Krucker, H. S. Hudson, L. Glesener, S. M. White, S. Masuda, J. P. Wuelser, and R. P. Lin, Astrophys. J. **714**, 1108 (2010).
[3] M. Øieroset, T. Phan, M. Fujimoto, R. P. Lin, and R. P. Lepping, Nature (London) **412**, 414 (2001).
[4] H. Che, J. F. Drake, and M. Swisdak, Nature (London) **474**, 184 (2011).
[5] V. Roytershteyn, W. Daughton, H. Karimabadi, and F. S. Mozer, Phys. Rev. Lett. **108**, 185001 (2012).
[6] M. Hesse *et al.*, Phys. Plasmas **25**, 122902 (2018).
[7] A. Le, W. Daughton, O. Ohia, L.-J. Chen, Y.-H. Liu, S. Wang, W. D. Nystrom, and R. Bird, Phys. Plasmas **25**, 062103 (2018).
[8] T. Speiser, J. Geophys. Res. **70**, 4219 (1965).
[9] V. M. Vasyliunas, Rev. Geophys. **13**, 303 (1975).
[10] L. Lyons and D. Pridmorebrown, J. Geophys. Res. **95**, 20903 (1990).
[11] R. Horiuchi and T. Sato, Phys. Plasmas **1**, 3587 (1994).
[12] H.-J. Cai and L. Lee, Phys. Plasmas **4**, 509 (1997).
[13] M. M. Kuznetsova, M. Hesse, and D. Winske, J. Geophys. Res. **103**, 199 (1998).
[14] J. L. Burch, T. E. Moore, R. B. Torbert, and B. L. Giles, Space Sci. Rev. **199**, 5 (2016).
[15] S. A. Fuselier *et al.*, J. Geophys. Res. **122**, 5466 (2017).
[16] J. L. Burch *et al.*, Science **352**, aaf2939 (2016).
[17] J. Egedal, A. Le, W. Daughton, B. Wetherton, P. A. Cassak, J. L. Burch, B. Lavraud, J. Dorelli, D. J. Gershman, and L. A. Avanov, Phys. Rev. Lett. **120**, 055101 (2018).
[18] R. B. Torbert *et al.*, Science **362**, 1391 (2018).
[19] T. D. Phan, J. F. Drake, M. A. Shay, F. S. Mozer, and J. P. Eastwood, Phys. Rev. Lett. **99**, 255002 (2007).
[20] M. Øieroset *et al.*, Geophys. Res. Lett. **43**, 5536 (2016).
[21] K. Bowers, B. Albright, L. Yin, W. Daughton, V. Roytershteyn, B. Bergen, and T. Kwan, J. Phys. **180**, 012055 (2009).
[22] See Supplemental Material at http://link.aps.org/supplemental/10.1103/PhysRevLett.123.225101 for details on optimizing the LMN-basis vectors, converting the VPIC units into units applied by the MMS spacecraft, determining the upstream parameters required for the simulation, and inferring the MMS trajectory through the simulation.
[23] B. U. Sonnerup and L. J. Cahill, J. Geophys. Res. **72**, 171 (1967).
[24] W. Daughton, J. Scudder, and K. Homa, Phys. Plasmas **13**, 072101 (2006).
[25] A. Le, J. Egedal, W. Daughton, W. Fox, and N. Katz, Phys. Rev. Lett. **102**, 085001 (2009).
[26] A. Le, J. Egedal, W. Daughton, J. F. Drake, W. Fox, and N. Katz, Geophys. Res. Lett. **37**, L03106 (2010).
[27] A. Le, J. Egedal, and W. Daughton, Phys. Plasmas **23**, 102109 (2016).
[28] J. Egedal, W. Daughton, J. F. Drake, N. Katz, and A. Le, Phys. Plasmas **16**, 050701 (2009).
[29] J. Egedal, M. Øieroset, W. Fox, and R. P. Lin, Phys. Rev. Lett. **94**, 025006 (2005).
[30] J. Egedal, W. Fox, N. Katz, M. Porkolab, M. Øieroset, R. P. Lin, W. Daughton, and J. F. Drake, J. Geophys. Res. **113**, A12207 (2008).
[31] L. J. Chen *et al.*, J. Geophys. Res. **113**, A12213 (2008).
[32] J. Egedal, A. Le, and W. Daughton, Phys. Plasmas **20**, 061201 (2013).
[33] A. Le, J. Egedal, O. Ohia, W. Daughton, H. Karimabadi, and V. S. Lukin, Phys. Rev. Lett. **110**, 135004 (2013).
[34] K. J. Genestreti *et al.*, J. Geophys. Res. **123**, 9130 (2018).
[35] R. Nakamura *et al.*, J. Geophys. Res. **124**, 1173 (2019).
[36] https://lasp.colorado.edu/mms/sdc/public/.